Lab on a Chip

A Dental Implant-on-a-Chip for 3D Modeling of Host-Material-Pathogen Interaction and Therapeutic Testing Platform

Journal:	*Lab on a Chip*
Manuscript ID	LC-ART-08-2022-000774.R1
Article Type:	Paper
Date Submitted by the Author:	23-Oct-2022
Complete List of Authors:	Dhall, Atul; University of Pennsylvania School of Dental Medicine Tan, Jun; Kansas State University Oh, Min Jun; University of Pennsylvania School of Dental Medicine Islam, Sayemul; Temple University Kim, Jungkwun; University of North Texas Kim, Albert; University of South Florida Hwang, Geelsu; University of Pennsylvania School of Dental Medicine,

ARTICLE

A Dental Implant-on-a-Chip for 3D Modeling of Host-Material-Pathogen Interaction and Therapeutic Testing Platform

Received 00th January 20xx,
Accepted 00th January 20xx

DOI: 10.1039/x0xx00000x

Atul Dhall[a], Jun Ying Tan[b], Min Jun Oh,[a,c] Sayemul Islam[d], Jungkwun Kim[b,e*], Albert Kim[d,f*], Geelsu Hwang[a,g,*]

The precise spatiotemporal control and manipulation of fluid dynamics on a small scale granted by Lab-on-a-Chip devices provide a new biomedical research realm as a substitute for in vivo studies of host-pathogen interactions. While there has been a rise in the use of various medical devices/implants for human use, the applicability of microfluidic models that integrate such functional biomaterials is currently limited. Here, we introduced a novel dental implant-on-a-chip model to better understand host-material-pathogen interactions in the context of peri-implant diseases. The implant-on-a-chip integrates gingival cells with relevant biomaterials - keratinocytes with dental resin and fibroblasts with titanium while maintaining a spatially separated co-culture. To enable this co-culture, the implant-on-a-chip's core structure necessitates closely spaced, tall microtrenches. Thus, a SU-8 master mold with a high aspect-ratio pillar array was created by employing a unique backside UV exposure with a selective optical filter. With this model, we successfully replicated the morphology of keratinocytes and fibroblasts in the vicinity of dental implant biomaterials. Furthermore, we demonstrated how photobiomodulation therapy might be used to protect the epithelial layer from recurrent bacterial challenges (~3.5-fold reduction in cellular damage vs. control). Overall, our dental implant-on-a-chip approach proposes a new microfluidic model for multiplexed host-material-pathogen investigations and the evaluation of novel treatment strategies for infectious diseases.

Introduction

Microfluidics has been embraced by various fields within biomedical research.[1, 2] Utilizing fabrication technologies from the microelectromechanical systems (MEMS) and semiconductor industries[2] enables precise control and manipulation of fluids at submillimeter scales, bringing several distinct advantages from conventional approaches. For example, it requires substantially smaller sample volumes, enables high-throughput analyses, and provides greater control over the spatiotemporal fluid dynamics at a lower cost. Since these advantages translate well in biomedical research, a microfluidic setting is often chosen to model microenvironments, intended to substitute *in vivo* studies; a highly engineered microfluidics platform, organ-on-a-chip, is a noteworthy approach in the recent trend.[3]

When mimicking cellular microenvironments, a co-culture model that depicts physiologically relevant behaviors is a better approach than simplistic 2D monoculture systems.[4] Indeed, several organ-on-a-chip systems already provided improved replication of tissue functionality in comparison to conventional 2D and 3D static cell culture systems. These include notable examples like gut-on-a-chip [5], liver-on-a-chip,[6] lung-on-a-chip,[7] bone-marrow-on-a-chip,[8] and eye-on-a-chip.[9] Additional prominent examples of on-chip systems include contact-lens-on-a-chip[10] and a foreign-body-response-on-a-chip.[11] Despite such innovations in microfluidics with mimicking various parts of the human body and the rise in the use of a range of medical devices (or implants) for human use, the applicability of microfluidic models that resemble the complex microenvironmental interactions among the host, material, and pathogen is currently limited.

Due to the marsupialization of the skin epithelium along with implants, the implant serves as a major conduit for pathogen mobilization.[12] In the absence of a robust tissue barrier, organisms populating the implant can penetrate through the epidermis into the soft tissue and ultimately invade bone trabeculae. Since the skin interface is the common failure point, it is increasingly important to better understand host-material-pathogen interactions. For example, the oral mucosal barrier is a layered tissue with an active microbiome that is heavily colonized and often subjected to repetitive trauma.[13]

a. Department of Preventive and Restorative Sciences, School of Dental Medicine, University of Pennsylvania, Philadelphia, PA 19104, USA.
E-mail: geelsuh@upenn.edu
b. Department of Electrical and Computer Engineering, Kansas State University, Manhattan, KS 66506, USA.
c. Department of Chemical and Biomolecular Engineering, School of Engineering and Applied Sciences, University of Pennsylvania, Philadelphia, PA 19104, USA.
d. Department of Electrical and Computer Engineering, Temple University, Philadelphia, PA 19122, USA.
e. Department of Electrical Engineering, University of North Texas, Denton, TX 76203, USA.
E-mail: jungkwun.kim@unt.edu
f. Department of Medical Engineering, University of South Florida, Tampa, FL 33620, USA.
E-mail: akim1@usf.edu
g. Center for Innovation & Precision Dentistry, School of Dental Medicine, School of Engineering and Applied Sciences, University of Pennsylvania, Philadelphia, PA 19104, USA.
* Corresponding authors
Electronic Supplementary Information (ESI) available: [details of any supplementary information available should be included here]. See DOI: 10.1039/x0xx00000x

Such microbial challenges to peri-implant soft tissue are one of the major components associated with the pathogenesis of peri-implant diseases.[14, 15] Notably, the prevalence of such osseointegrated dental implants in the US is projected to reach as high as 23% by 2026 with an aging population,[16] elevating implant complications due to the popularity of dental implants.[17, 18] As establishing a peri-implant soft tissue seal to the implant to prevent its failure from microbial insult is critical,[19] there is considerable interest in studying host-material-pathogen interactions in the oral environment. However, no microfluidic models are presently available for studying the behaviors of the peri-implant soft tissue microenvironment in relation to biomaterials, such as dental resin and titanium (i.e., two major components of dental implants). Given the advantages of microfluidic co-culture models, the rise in modular microfluidics, and the past successes of organ-on-a-chip systems, a microfluidic model to replicate the functionality and cellular architecture around a dental implant can be highly beneficial to our understanding of host-material-pathogen interactions in the context of peri-implant disease.

Here, we present the first dental Implant-on-a-Chip (IOC), a physiologically relevant *in vitro* model, for investigating host-material-pathogen interactions as a proof of concept. While cell-to-cell interactions in the context of various organ functions could be implemented in a typical organ-on-chip, integrating biomaterials into the microfluidic model can be technically challenging as the microchannels should provide sufficient space (especially height) to accommodate materials within the chip. Furthermore, two microchannels shall be separated by a porous membrane with small, closely spaced yet tall pores to culture distinct cell types. To overcome this hurdle, we adapted our previously reported backside UV lithography[20] to enable unprecedented high-aspect-ratio microchannels separated by closely spaced, tall, elliptical micropillars (replacing a porous membrane). We also employed a modular strategy for the incorporation of dental materials (such as dental crown resin and titanium implant post), which can be used for other applications. Through this, we successfully fabricated high-aspect-ratio SU-8 layers and resultant PDMS microchannels that have one side wall enclosed by biomaterials such that human gingival keratinocyte and fibroblast (HGKs and HGFs, respectively) populations interface with their respective dental materials (crown for HGKs and titanium for HGFs), mimicking the entire dental implant microenvironment. We verified our design via modeling the fluid dynamics within the IOCs to demonstrate minimal mixing between cell culturing microchannels while allowing cross-talking, leading to conducive growth conditions for both cell populations. After optimizing cell culture conditions within the IOCs, we challenged the keratinocyte layer with an oral pathogen, *Streptococcus mutans,* to mimic a bacterial insult. Furthermore, we tested the efficacy of photobiomodulation (PBM) therapy using this IOC to demonstrate its applicability as a therapeutic testing platform. We observed that microbial insult severely damaged HGKs, while PBM therapy effectively protected HGKs, exhibiting a ~3.5-fold lower loss in HGK in comparison to controls without PBM treatment. Overall, our IOCs represent a physiologically relevant *in vitro* model of the cellular microenvironment for the investigation of host-material-pathogen interactions and a therapeutic testing platform.

Material and methods

General recipe for PDMS

Polydimethylsiloxane (PDMS - Sylgard® 184, Dow Silicones Corporation, Midland, MI, USA) was prepared by mixing 10:1 wt % of base:crosslinker. The uncured polymer was poured over the SU-8 master molds, degassed for 30 min, and cured on a hotplate at 70 °C for 3 h.

Computer-aided design

All designs for the microfluidic layers, the constituent parts (dental resin block and titanium block), the geometries for fluid dynamics simulations and the custom chip-holder for photobiomodulation experiments were made in Autodesk® AutoCAD 2019.

Fabrication of master molds for microfluidic layers and dental resin blocks

Two-by-two-inch chromium-coated photomasks (Telic Company, Santa Clarita, CA, USA) were drop-coated uniformly with 840 mg of SU-8 2025 (Kayaku Advanced Materials, Inc., Westborough, MA, USA). The weight of the 840 mg indicated the master mold's thickness to be 210 µm after the soft baking process. This thickness of SU-8 was enough to ensure that the blocks remained rigid and could be handled without bending during chip assembly. The photomasks were then transferred to a conventional hotplate for a two-step soft-baking process: the hotplate was scheduled to heat up from 25 to 70 °C for 7 min and then from 70 to 95 °C for 40 min. After completing the soft-baking process and cooling the samples, they were exposed to broadband UV using a commercial UV exposure tool (Model 30 UV light source, Optical Associate Inc., Milpitas, CA, USA). For a total exposure time of 50 s, a constant UV intensity of 30 mW/cm^2 was applied. The samples were then returned to the hotplate for post-exposure bake (PEB) at temperatures ranging from 25 to 45 °C for 2 min, 45 to 65 °C for 3 min, and lastly 65 to 95 °C for 15 min. After completing the PEB and cooling the samples, they were immersed in SU-8 developer (Kayaku Advanced Materials, Inc.) for 10 min. Following that, samples were cleaned with isopropyl alcohol (IPA), dried using compressed air, and carefully stored for experimental use. The same procedure was utilized to create the master molds for the dental resin blocks, only a one-inch by one-inch photomask was employed.

Fabrication of dental resin blocks

PDMS was used as an intermediate in replica molding of the master molds for dental resin blocks (Supplementary Fig. S1). After curing, PDMS samples were peeled away and cleaned with scotch tape and IPA. Samples were then dried with compressed air. Precured, biocompatible Class IIa dental resin (C&B MFH, Next Dent B.V., Netherlands) was poured into slots within the PDMS molds. To obtain a uniform surface, a piece of UV transparency film (Apollo, ACCO Brands, Lake Zurich, IL) was gently placed onto uncured dental resin while releasing air bubbles. A UV LED flashlight with an irradiance of 4 mW/cm^2 (V1 385 -395 nm, uvBeast, Portland, OR, USA) was used to cure the dental resin blocks for 5 min. The transparency films were removed, and the blocks were rinsed with IPA and stored for experimental use. Resultant dental resin blocks were measured with a caliper with 0.01 mm resolution (Fowler, Canton, MA, USA) and found to be 230 ± 19 µm thick (Supplementary Fig. S2).

Fabrication of titanium blocks

The fabrication process was comparable to that for SU-8 mastermolds described previously with the following differences. 420 mg of SU-8 2025 was equally drop-coated onto one-inch by two-inch photomasks (Supplementary Fig. S3). After rinsing the samples with IPA to remove any remaining SU-8 developer, the samples were gently pressed to delaminate them from the photomask. The delaminated SU-8 samples were dried with compressed air and titanium metalized for 42 min at a deposition rate of 12 nm/min using a DC sputter (Korvus Technology, Maidenhead, UK) resulting in a final thickness of 500 nm. On the reverse side of the samples, the identical metallization procedure was performed. The metalized samples were then dried with compressed nitrogen and stored safely for experimental use. Resultant titanium blocks were measured with a caliper and found to be 217 ± 6 µm thick. (Supplementary Fig. S2).

Microfluidic chip assembly

Microfluidic layers of PDMS were fabricated from master molds using the general procedure described in Section 4.1. Biopsy punches (1 mm diameter) were used to create inlets and outlets. PDMS microfluidic layers were cleaned with scotch tape and IPA, followed by a 15 min sonication in Milli-Q water (MilliporeSigma, Burlington, MA, USA). In parallel, glass slides were rinsed with IPA and sonicated with Milli-Q water. The constituent parts of the modular microfluidic chips – dental resin and titanium blocks, were then placed into slots within the microfluidic layers using the corners and curves of these blocks as alignment marks. A flat spatula was used to gently spread uncured PDMS onto the interface between the blocks and microfluidic layers that were farthest away from the cell culture chambers (to avoid clogging the channels and chambers of the microfluidic chip). These composites of microfluidic layers with embedded blocks were placed in an oven at 100 °C for 2 min to cure the coating of PDMS. Finally, these composites were permanently bonded to glass slides using a plasma cleaner (PDC-32G, Harrick Plasma Inc., Ithaca, NY). Sealed chips were then sterilized under UV for 1 h and stored for experimental use.

Computational fluid dynamics

In order to predict and investigate flow characteristics in the microfluidic chip, the 2D finite element analysis (FEM) was performed with COMSOL Multiphysics software (V 6.0, COMSOL Inc., Burlington, MA). Physics-controlled mesh with extremely fine element size is created by the COMSOL built-in meshing method. All the physical properties of the water in the microfluidic chip are used directly from the COMSOL materials library. The thickness of the microfluidic channel is 210 µm, the temperature is 37 °C, and the flow rate is 0.3 µL/min for each inlet. For rectangular microfluidic channels, shear stress can be derived as follows[21] when the length of the channel is much greater than the height and width:

$$\tau = \frac{6\mu Q}{h^2 w}$$

where τ is the shear stress, µ is the dynamic viscosity, Q is the flow rate, h is the height of the channel and w is the width of the channel. For each cellular chamber in the IOC, with h = 200 µm and w= 600 µm, the calculated shear stress was 0.009 dyn/cm^2.

The stationary study of the Laminar Flow module is conducted to simulate the incompressible steady-state flow profile in the microfluidic chip. The time-dependent study of Transport of Diluted Species Modules and previous stationary study solutions were used to account for the mass transfer between upper and lower channels. Inlet 1 is filled with a higher concentration (1 mol/m^3), while inlet 2 is filled with a lower concentration (0 mol/m^3). For the concentration of diluted species, 1 mol/m^3 at inlet 1 and 0 mol/m^3 at inlet 2 are applied. The simulations accounting for the limited transport of sub-micron-sized bacteria from the upper channel to the lower channel in presence of a flow were conducted using the Particle Tracing Module and previous stationary study solutions. A 0.5 µm of particle diameter and an 1100 kg/m^3 of particle density are used to mimic bacteria cells. The sub-micron-sized particles were uniformly released over a 2500 s period at inlet 1, 100 particles at a time, with a total number of particles of 100,000.

Experimental validation of small particle transport

To experimentally validate the minimal mixing nature of small particles flowing through the IOC, we conducted a time-series experiment with GFP-labeled *S. mutans* UA159. Briefly, bacteria-laden solution (~10^6 CFU/mL in PBS) was flown through the upper chamber (meant for keratinocytes) at 0.3 µL/min. Simultaneously, bacteria-free PBS was flown through the lower chamber (meant for fibroblasts) at 0.3 µL/min. Snapshots of the central part of the IOC were taken at 0, 1, 2, and 4h with a Leica DMi8 (Leica Microsystems, Deerfield, IL, USA).

Cell culture in chip and continuous flow experiments

HGKs (kindly provided by the laboratory of Dr. Dana T. Graves, School of Dental Medicine, University of Pennsylvania) and HGFs (kindly provided by the laboratory of Dr. Jonathan Korostoff, School of Dental Medicine, University of Pennsylvania) were used for all experiments. Cells were maintained in their respective culture media (HGKs: Keratinocyte Basal Medium (KBM-Gold, Lonza Group AG, Basel, Switzerland) supplemented with KGM-2 SingleQuots kit (Lonza); HGFs: Fibroblast Basal Medium (ATCC, Manassas, VA, USA) supplemented with Fibroblast growth kit (ATCC, PCS-201-041) and 1% v/v Anti−Anti (Gibco, Gaithersburg, MD, USA)) and incubated at 37 °C in a humidified atmosphere of 5% CO_2 until confluence. Before seeding chips with cells, 50 µg/mL of collagen type I (Sigma-Aldrich, St. Loius, MO, USA) was flown through the chips at 0.3 µL/min for 1 h (Dual NE-4000 Syringe Pumps, New Era Pump Systems Inc., Farmingdale, NY, USA) to coat the glass slides and make them conducive substrates for HGK and HGF attachment. 10,000 cells/mL of each cell type were then flown into their respective chambers at 0.3 µL/min and flow was stopped for 4 h to allow initial adhesion of cells to the collagen-coated glass slides. After initial adhesion was confirmed, the flow of respective media was maintained in the chambers for 3 days at 0.3 µL/min until both populations of cell types were confluent in their respective chambers.

Fabrication of PBM platform

To mimic PBM therapy in the microfluidics chip, a custom chip holder was designed and 3D printed (Form 2, FormLabs, Somerville, MA, USA). Our custom chip-holder was a miniaturized form of a LED platform that we have previously optimized for use in host-pathogen investigations.[22] Briefly, red LEDs (λ = 615 nm; SML-P12U2TT86R, ROHM Semiconductor, UK) were used on a miniaturized LED platform that was fabricated by connecting a resistor in series with an LED (1.2 kΩ) to limit the current and protect electronics. Irradiance was kept consistent with our previous study[22] by using the irradiation profile in Supplementary Fig. S4. After the LED circuit was assembled on a printed circuit board, it was placed in a slot of a 3D printed block, followed by electrical and thermal passivation by 3D printing resin. Using insulated wires (29 AWG), the LED circuit was connected to a power supply as described previously.[22]

Bacterial challenge and photobiomodulation experiments

S. mutans UA159, a cariogenic oral pathogen, was used for bacterial challenge experiments. Stocks were stored at −80 °C in tryptic soy broth containing 50% glycerol. Strains were grown to the mid-exponential phase in ultrafiltered (10 kDa molecular-mass cutoff; Millipore, Billerica, MA, USA) tryptone-yeast extract broth (UFTYE; pH 7.0) containing 1% glucose.[23, 24] Cells were harvested by centrifugation (5500g, 10 min, 4 °C). *S. mutans* UA159 was transferred from stock culture to the culture medium (UFTYE containing 1% glucose) and incubated overnight at 37 °C and 5% CO_2. From this culture, bacteria were transferred onto a fresh culture medium and incubated at 37 °C and 5% CO_2 to mid-exponential phase (optical density of 1.0 at 600 nm corresponding to $2x10^9$ CFU/mL). After confluency was attained for both cells on day 3, the chips were placed in custom chip holders and subjected to LED treatment for 90 minutes. Control chips were placed in the chip holders but not subjected to LED treatment. An optimized density of $7x10^6$ CFU/mL of *S. mutans* was added to antibiotic-free KBM-Gold cell culture media and bacteria-laden media was flown through the HGK chamber for 24 h. Images of 3 random areas (representing 50% of the width of the cell chambers) of cells in both chambers were taken at 0 and 24 h (representing before and after bacterial challenge). To assess the growth of *S. mutans* in the input media, the number of viable bacterial cells (CFU/mL) in the input reservoir was determined at 0 and 24 h by taking out 400 µL of the reservoir at these time points and plating it on blood agar plates (BD BBL Prepared Plated Media: Trypticase Soy Agar (TSA II) with Sheep Blood, Thermo Fisher Scientific, Waltham, MA, USA). All experiments were conducted 3 times resulting in a total of 9 before-after image pairs and 6 CFU/mL counts per condition.

Staining, imaging, and quantification

Cultured HGKs and HGFs were fixed using 4% paraformaldehyde solution (Santa Cruz Biotechnology, Inc., Dallas, TX, USA) for 15 min at 37°C and then rinsed with PBS three times for 5 minutes each. Once fixed, cells were permeabilized with 0.1% Triton X-100 (Sigma-Aldrich) in PBS for 10 min at room temperature, followed by three 5-min rinses with PBS. Cells were then stained with Dylight™ 650 Phalloidin (Cell Signaling Technology, Danvers, MA, USA; Ex/Em: 651/672nm) diluted 1:20 in PBS for 15 minutes at room temperature in the dark and then rinsed once with PBS. Finally, cells were stained with DAPI (Invitrogen, Waltham, MA, USA; Ex/Em: 358/461nm) using 1µg/ml of PBS for 5 minutes at room temperature in the dark and then rinsed once with PBS. Immediately after completion of staining, cells were then imaged using a confocal microscope (LSM800, Zeiss, Jena, Germany) at 10X.

Master molds for microfluidic layers and titanium blocks were imaged using a digital microscope (Smartzoom 5, Zeiss, Jena, Germany). SEM images were taken with a PS-210 (PEMTRON Co. Ltd., Seoul, South Korea). Top view images of PDMS microfluidic layers were taken with a Zeiss Axiovision microscope (Zeiss). Cell culture images were taken with a Nikon TMS inverted phase-contrast microscope (Nikon Inc., Melville, NY< USA) fitted with a camera at 10X. Surface area coverage, raw cell number, and cell size for each image were estimated using ImageJ (Fiji[25]) and its cell counter plugin, respectively. Surface coverage was compared between the IOC and culture flasks, and between different regions within the IOC, using ImageJ. By normalizing values to those from 0 h images, the percentage drop in surface area coverage and percentage drop in cell number were estimated.

Statistical analysis

All experiments were conducted at least three times with all data represented as mean ± SD. GraphPad Prism was used for all statistical analyses. Significant differences in data were assessed using unpaired t-tests with a significance level set to $p < 0.05$.

Results

IOC design and assembly

Typical organ-on-chip allows culturing of distinct cell types in the top and bottom microchannels that are separated by a porous membrane (as a representative of the cell membrane). Embedding biomaterials into a microfluidic device, especially to interface with cells, requires significant modification to the overall design, including microchannel orientation, dimension, and cell membrane-mimicking porous membrane. The IOC is designed to mimic the microenvironment in the vicinity of a dental implant (Fig. 1A-C). As illustrated, two representative dental implant components, i.e., dental resin and titanium, are faced with two types of gingival soft tissues, HGKs (Fig. 1D) and HGFs (Fig. 1E).

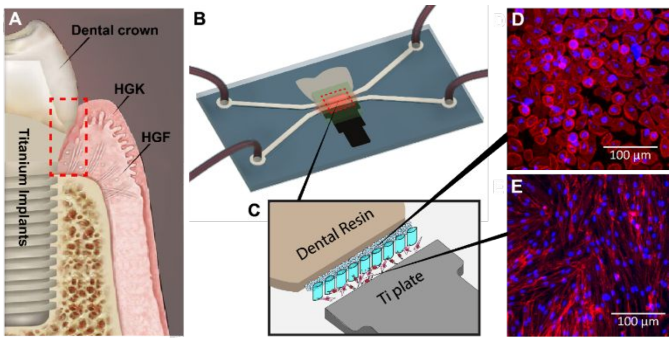

Fig. 1. Implant-on-a-chip (IOC) for *in vitro* modeling of interactions between peri-implant soft tissues and implant components. (A) Illustration of dental implants and nearby soft tissues. (B) schematic design of IOC, mimicking dental implant microenvironment. (C) Close-up view of microfluidic channels separated by elliptical micropillars; dental resin and titanium plate are integrated into the IOC while facing human gingival keratinocytes (HGKs) and fibroblasts (HGFs), respectively. Representative confocal images of (D) HGKs and (E) HGFs, displaying high confluence. Blue: Cell nuclei stained with DAPI; Red: Actin filaments stained with Phalloidin.

As the dental IOC structure is PDMS-converted from the SU-8 master mold, the SU-8 lithography performance is highly reliant on process parameters to achieve high-resolution, stable microstructures,[26] which must be fine-tuned to get optimal results. The overall height was designed to be >200 µm mainly to seamlessly accommodate the dental materials, and the microchannel width was set to 600 µm. To integrate biomaterials in a modular manner, the cell culturing space (middle of the IOC) was designed to be large void spaces, which were later inserted with the material and formed seamless microchannels aligned with the inlet and outlet. Figure 2A-F illustrates the fabrication process of the master mold for the IOC. To prepare the mold, CAD of the photomask (Fig. 2G) was prepared and chromium-coated photomasks were drop-coated uniformly with SU-8 2025, followed by a two-step soft-baking process. It resulted in the master mold's thickness being ~210 µm. Then, the mold was exposed to broadband UV for 50 s at a constant intensity of 30 mW/cm^2. After completing the three-step post-exposure bake (PEB) and immersing in SU-8 developer for 10 min, the master mold was prepared. SEM images of the SU-8 microstructures showed the separation between the elliptical microtrenches (Fig. 2H) and top and side views of a SU-8 mold on glass depicted achieved average wall size and SU-8 thickness (Fig. 2I).

A similar procedure was utilized to create the master molds for the dental resin and titanium blocks. Supporting Information (Figs. S1 and S3) illustrates the overall process of fabricating dental resin and titanium blocks. The tooth-shaped dental crown material is fabricated from commercial crown resin (Supplementary Fig. S1). Similarly, the titanium implant post is shaped like a screw (Supplementary Fig. S3). Apart from the aesthetic resemblance to a dental implant, the primary purpose of the curvatures in the dental resin and titanium blocks was to serve as alignment marks during the IOC assembly. Microfluidic layers of PDMS were fabricated from master molds, and biopsy punches (1 mm diameter) were used to create inlets and outlets. Fig. 3A-G illustrates the assembly of the IOC. After cleaning, prepared dental resin and titanium blocks were placed into slots within the microfluidic layers. Uncured PDMS was spread onto the interface between the blocks and microfluidic layers to create tight sealing. The composite of the microfluidic layer with embedded blocks was placed in an oven to cure the coating of PDMS; in turn, the composite was permanently bonded to glass slides using a plasma cleaner. Fig. 3H-N show the images of a PDMS microfluidic layer, depicting 14 elliptical micropillars separated by 10 µm pores to segregate channels for distinct cell types. A picture of the PDMS microfluidic layer without dental resin and titanium blocks is shown in Fig. 3O, and the composite microfluidic layer with PDMS and blocks is shown in Fig. 3P. The IOC was ready for use in proof-of-concept host-material-pathogen investigations.

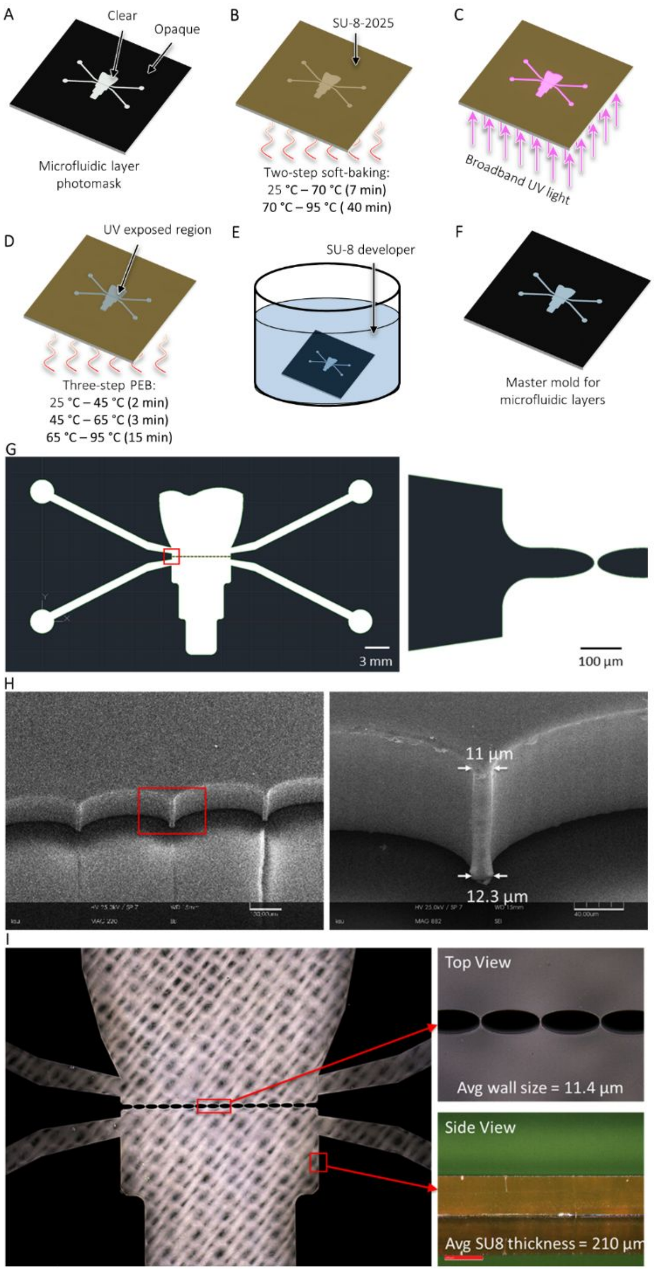

Figure 2. Schematic diagram for master mold fabrication and the SU-8 master mold used to form microfluidic layers. (A) Chromium-coated photomask. (B) Soft-baking process. (C) Exposure to broadband UV. (D) Post-exposure baking process. (E) Immersion into SU-8 developer. (F) Final SU-8 master mold. (G) CAD of the photomask. Inset: Zoomed-in version of the elliptical microstructures. (H) SEM image of the SU-8 microstructures. Inset: Zoomed-in image of the separation between the elliptical microtrenches. (I) Top view of a SU-8 master mold. Insets: Zoomed-in top and side views depicting average wall size and SU-8 thickness.

Optimization of cell culture

The ability to cultivate two unique cell types in a microfluidic chip without physical mixing while permitting cross-talk is the key to mimicking host-pathogen interaction *in vitro*. A crucial benefit of conducting experiments in microfluidic settings is the predictable behavior of the fluid dynamics with laminar flow.[2] Given that the IOC should generate spatially separated cell populations of HGKs (in the upper chamber for top view) and HGFs (in the lower chamber for top view), it was imperative to study fluid dynamics within the IOC prior to biological testing. Thus, we ran computational fluid dynamics (CFD) simulations (COMSOL Multiphysics®, COMSOL; see Material and methods for details) in the microchamber (Fig. 4A). Additionally, it was important to ensure that we used an optimal flow rate during the experiments. Based on the limited existing literature available from microfluidic models (involving keratinocytes[27] and fibroblasts[28]), we established an optimal flow rate of 0.3 µL/min for cell experiments in the IOC. It is well-known that keratinocytes are extremely mechanoresponsive and start showing morphological variation and cytoskeletal reorganization with as little as 0.06 dyn/cm^2.[29] Thus, our intention was to minimize all morphological variations induced by the flow of nutrient media and focus on co-culturing cells with implant materials under dynamic settings. The resultant shear stress in the microfluidic channels was 0.009 dyn/cm^2. Overall, our microchambers design with 10 µm pores microtrenches exhibited highly suitable laminar flow paths with minimal mixing at a flow rate of 0.3 µL/min. We also simulated the effect of the specimen size with two different sizes of molecules/particles (Fig. 4B-D). By flowing small molecules through inlet 1, using a diffusion coefficient of glucose in water at 37 °C (9.59 × 10^{-10} m^2/s),[30] we observed that the molecules started to mix as soon as they entered the microchamber, which continued toward the outlets over time (Figure 4B, D). In contrast, when particles with 0.5 µm diameter were released from inlet 1, they did not appear in outlet 2, indicating no significant mix regardless of spatial or temporal stimulation (Fig. 4C, D). In other words, the simulation results clearly justify that the pore width (10 µm) chosen for the IOC chip can resemble the cell membrane function (allowing each cell to access their respective nutrient media without chaotic mixing while serving as a protective barrier for underneath tissues from other organisms such as bacteria), suitable for the subsequent biological experiments. To experimentally validate the minimal mixing nature of the IOC with small particles, bacteria-laden solution (GFP *S. mutans*) was flown through the upper chamber (meant for keratinocytes) while a bacteria-free solution was flown through the lower chamber (meant for fibroblasts) at 0.3 µL/min. As clearly demonstrated in Supplementary Fig. S5, bacterial cells predominantly remain within the chamber through which they were introduced (keratinocyte chamber). There is minimal mixing of these particles into the fibroblast chamber. This information along with Fig. 4F and G distinctly proves that the porous membrane in our IOC can be used to avoid mixing of the solutions in the two chambers, allowing us to have spatially separate co-cultures of different cell types (similar to human physiology) and selectively challenge the epithelial cells in our model with relevant bacteria.

The CFD simulation was verified by culturing HGKs and HGFs within the chips for continuous flow experiments. We cultured both HGKs and HGFs in their respective chambers while interfacing with models of dental crowns (dental resin blocks) and titanium posts (titanium blocks). As shown, an input flow rate of 0.3 µL/min and cell seeding density of 10,000 cells/mL ensured a homogenous distribution of spatially separated cell populations in their respective chambers on day 0 (Fig. 4E). Over the next 3 days, HGKs formed close

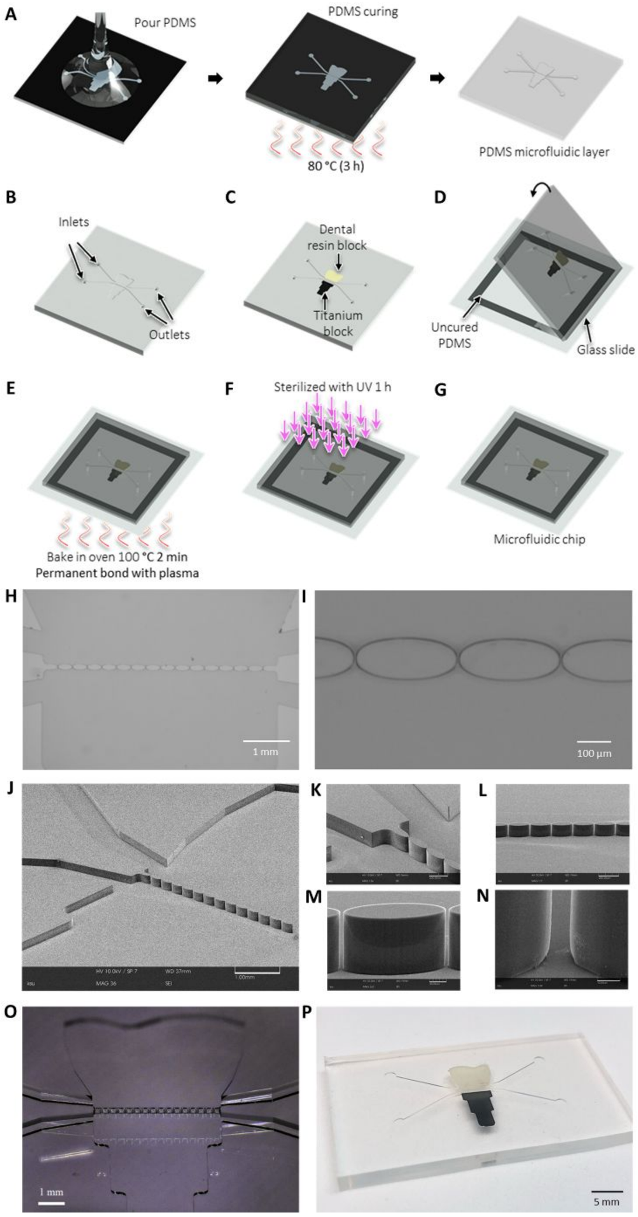

Fig. 3. Assembly of the implant-on-a-chip (IOC) and components for the modular assembly of the IOC. (A) Addition of uncured PDMS to the master mold followed by curing and release of the PDMS microfluidic layer. (B) Creation of inlets and outlets. (C) Embedment of dental resin and titanium blocks with a coating of PDMS. (D) Curing of the PDMS coating and (E) plasma bonding of the PDMS layer to glass. (F) Sterilization of the IOC. (G) Assembled IOC ready for experimental use. (H) Image of a PDMS microfluidic layer depicting 14 elliptical micropillars separated by 10 µm pores. (I) Zoomed-in image of the pores. (J) SEM image of the PDMS microfluidic layer with (K) zoomed-in versions and (L), (M), and (N) depicting sequentially larger magnifications of side-on views. (O) Image of the PDMS microfluidic layer without dental resin and titanium blocks. (P) Composite microfluidic layer with PDMS and blocks.

cell-cell contacts to form a monolayer of confluent epithelial cells in the proximity of the dental resin block (Fig. 4F). Similarly, HGF chambers interfacing with titanium block were confluent with elongated morphology by day 3 (Figure 4G). Excitingly, we found that there were no significant differences in cell densities between IOC and a traditional cell culture flask (Supplementary Fig. S6). Furthermore, quantified local cell densities nearby dental blocks and the middle of each chamber revealed that dental resin and titanium blocks did not compromise the colonization of HGKs and HGFs, respectively (Fig. 4H). In fact, both cell types were seen to be in direct contact with and conform to their respective material from top-down images (Supplementary Fig. S7). These are strong indicators that both cell populations adjusted well to their environment in the IOC. Our results represent the first demonstration of interfacing hard dental materials of an implant with epithelial and connective tissue cells in a microfluidic setting. These results established our model as a suitable platform for conducting host-pathogen investigations in physiologically relevant settings.

Bacterial challenge and photobiomodulation

Once our cell culture conditions were optimized, we performed proof-of-concept bacterial challenge experiments and tested the protective ability of PBM therapy within our system. In our previous study, we investigated the effects of blue, green, red, and near-infrared light on HGKs numbers that were infected with lipopolysaccharides.[22] We observed that red or near-infrared light significantly increased cell numbers relative to non-irradiated controls.[22, 31] In contrast, green light did not affect cell proliferation, whereas blue light caused extensive photocytotoxicity.[22] To corroborate our previous findings of the protective effect of PBM therapy on keratinocytes and to demonstrate the amenability of our system with PBM-based investigations, we utilized red light and tested chips under two conditions – with and without LED treatment before the bacterial challenge. For LED treatment, the chips were placed in custom chip-holders designed for near-contact PBM therapy (Figure 5A, B).

To mimic bacterial challenge in the oral cavity, *Streptococcus mutans* was added to antibiotic-free HGK nutrient media, and those media were used to challenge the HGK layer for 24 h. By testing various densities of *S. mutans*, we found that flowing lower than ~1x10^6 CFU/mL of *S. mutans* at the flow rate of 0.3 µL/min did not cause severe damage to HGKs (Supplementary Fig. S8). Seeding densities of ~7x10^6 CFU/mL of *S. mutans* induced severe loss of HGKs, thus it was chosen for the bacterial challenge experiment. Higher seeding densities of ~2x10^7 CFU/mL produced an extremely high loss of cell coverage (Supplementary Fig. S8) and were disregarded for bacterial challenge experiments. Representative images at 0 and 24 h demonstrated that HGK monolayers appeared to be less confluent and showed limited cell-cell contact when cultured with *S. mutans* without PBM treatment (Fig. 5C, D) while there was an insignificant increase in the average cell size for keratinocytes (~0.1%) (Supplementary Fig. S9). In contrast, PBM-treated HGKs already showed increased confluence before microbial challenge and exhibited minimal damage against *S. mutans* infection for 24 h (Fig. 5E, F). A set of 9 before-after image pairs per condition were used for quantification of the percentage drop in cell surface coverage (Fig. 5G) and cell number (Figure 5H). Overall, loss of cell surface coverage was 3.5-fold greater in control chips in comparison to LED-treated

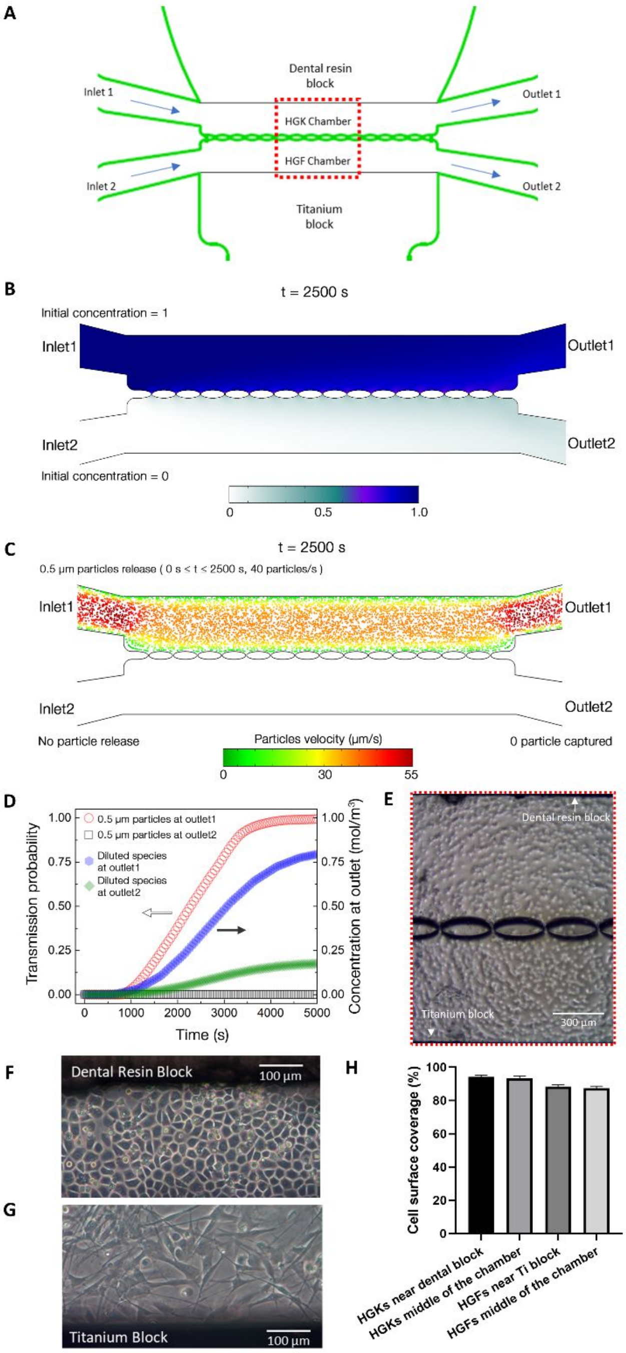

Fig. 4. Cell culture within IOCs. (A) Schematic of the fluidic environment of the IOC with separate chambers for HGKs and HGFs. (B) Simulation of small molecules flowing in via inlet 1. (C) Simulation of 0.5 µm particles entering via inlet 1. (D) Concentration at outlet and transmission probability vs time. (E) 4X image of HGKs and HGFs after seeding demonstrated a homogenous distribution of spatially separated cell populations. (F) Representative 10X image of HGKs in their chamber and their interface with dental resin blocks. (G) Representative 10X image of HGFs in their chamber and their interface with titanium blocks. (H) Comparison of cell surface coverage at different locations within the chambers.

chips. This was a direct consequence of a significant number of cells being detached in the control chips due to bacterial insult for 24 h. Accordingly, there was a 2.5-fold greater drop in cell number for control chips in comparison to LED-treated chips. To confirm that there was bacterial growth during the challenge, we quantified the CFU/mL of *S. mutans* in the input reservoir at 0 and 24 h. In both control and LED-treated conditions, there was a 1 log increase in CFU/mL and visible turbidity in the reservoir after 24 h, indicating that light irradiation can boost HGKs in resisting recurrent bacterial challenges up to ~5×10^7 CFU/ml of pathogens (Fig. 5I). Our results indicated that LED treatment was beneficial for the HGKs layer.

As further proof of the laminar nature of the fluid dynamics of our system, we also imaged the HGF layer at 0 and 24 h post bacterial challenge to the HGK layer (Supplementary Fig. S10). Encouragingly, we noticed no significant damage to the HGF layer after bacterial challenge in either of the chips (control or LED-treated). This validated the minimal mixing between the spatially separated cell populations within the IOC as well as the unique characteristics of keratinocytes as a protective barrier against bacterial challenges. Overall, our results highlight the IOC as a novel, modular, microfluidic platform to conduct physiologically relevant host-pathogen interactions and assess the feasibility of strategies such as PBM therapy.

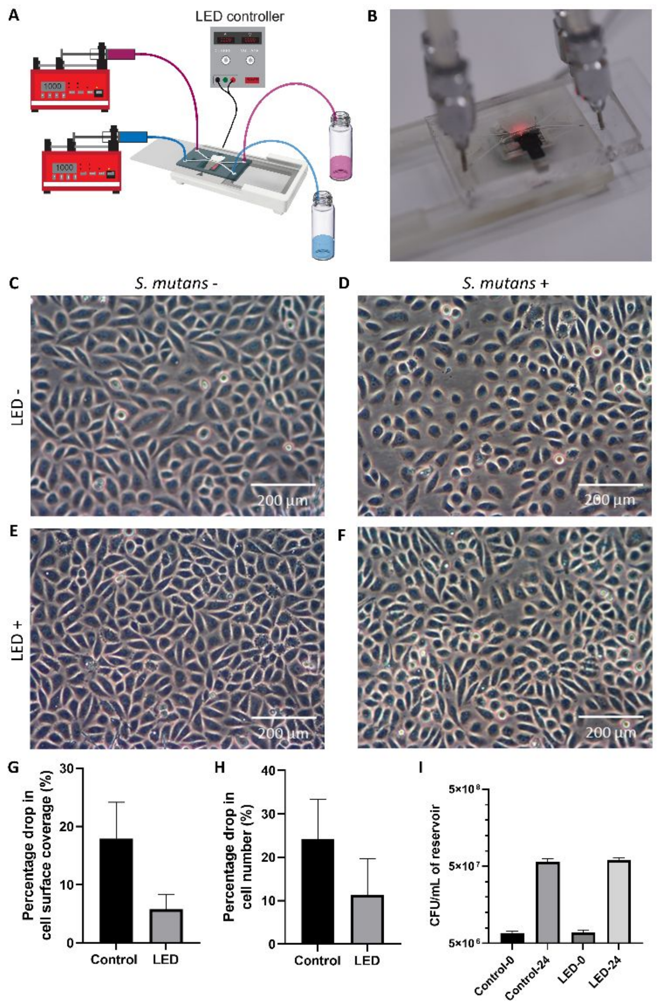

Fig. 5. Bacterial challenge to HGK layers and PBM therapy. (A) Schematic of a flow experiment in the IOC in conjunction with PBM therapy. (B) Close-up view of the IOC during a bacterial challenge experiment with PBM therapy. *S. mutans* was used to challenge HGK layers of control and LED-treated chips. Representative images of HGKs in control chips at (C) 0 h and (D) 24 h. Representative images of HGKs in LED-treated chips at (E) 0 h and (F) 24 h. Percentage drop after 24 h in (G) cell surface coverage and (H) cell number for control and LED-treated chips. (I) CFU/mL of the input reservoir at 0 and 24 h for control and LED-treated chips * represents t-tests with $p < 0.05$; (n>3).

Discussion

Microfluidic physiological systems have garnered tremendous interest in recent years because of their usefulness in providing novel insights into normal human function and their potential to be informative for the discovery and development of therapeutic strategies.[32-34] Although animal models have been useful in improving our understanding of the physiology and pathogenesis of diseases, these models are generally expensive and time-consuming but poorly predict human physiology, particularly for drug development.[35] As such, there has been a constant and undeniable need for models that more accurately predict human responses.[36] However, due to ethical concerns and the limitation of invasive procedures, collecting tissue samples from human subjects is often extremely difficult or impossible. Notably, microfluidics technologies offer a powerful screening platform for healthcare monitoring and therapeutics by replicating *in vivo* conditions with the low-cost and rapid fabrication of the chip.[37-39] With significant advances in microfabrication, dynamic *in vitro* systems are increasingly gaining traction as relevant models of tissue microenvironments.

Such microfluidic models can be highly beneficial for dental research because the oral cavity is a representative part of the human body that harbors a diverse array of organisms, including microbes and soft/hard tissues, and microfluidic models can enable precise spatiotemporal assessments of those interactions.[40] Recently, another component, biomaterials in a denture or implant, was added into those interactions, which serve an essential role in local and systemic health. However, microfluidic models have been employed infrequently in dental research so far. While some studies introduced microfluidics to investigate the oral environment, these studies focused on either the oral mucosa or the dentin-pulp interface.[27, 41-44] For example, Franca *et al.* developed and validated a tooth-on-a-chip platform to replicate the pulp–dentin interface and study the dental pulp cell response to biomaterials.[42] Subsequently, Rodrigues *et al.* used the tooth-on-a-chip platform to model the biomaterial-biofilm-dentin interface using *S. mutans* to test the antimicrobial efficacy of calcium silicate cement.[44] Similarly, as a proof-of-concept, *S. mutans* has been used to test bacterial invasion on keratinocytes in an oral mucosa-on-a-chip model.[43] Importantly, none of these studies represent models of host-material-pathogen interactions for dental implants. With modular microfluidics becoming increasingly prevalent, studying these interactions around dental implants using microfluidics is a logical progression and can significantly improve our biological understanding of the oral environment.

The osseointegrated implant is one of the important areas for human health where material-cellular interactions play critical roles. In the oral environment, the gingival tissue that surrounds a tooth/implant is composed of epithelial cells and connective tissue. Unlike tight seals around natural teeth in a healthy individual, incomplete tissue sealing around an implant leaves it more vulnerable to bacterial infiltration and subsequent cellular inflammation.[45] Such peri-implant diseases could lead to destructive failures, resulting in discomfort, painful and costly surgical replacement of failed implants, and the potential breakdown of the overall oral health.[46-48] This provides a strong justification for investigations of host-material-pathogen interactions that improve our understanding of the biology involved. Although dental implant surface properties play important roles in the inflammatory response of the adjacent peri-implant mucosal tissue, this has not been explored using microfluidic models yet.

Here, we have developed the first instance of a microfluidic implant on a chip system. In order to mimic the cellular environment around a dental implant, it is important to establish epithelial (HGKs) and connective tissue (HGFs) layers that interface with dental materials. However, developing a microfluidic environment with dental materials adds complexities to the fabrication strategy and protocol. Typically, microfluidic chips for biological experiments are required to have much wider microchannel dimensions for reliable large population cell culture than those for chemical assays.[49, 50] Furthermore, it is critical to have sufficient channel height to incorporate biomaterials (with hundreds of micrometers in thickness) into microfluidic chips. Although large channel width dimensions can be easily achieved (often up to 1 mm wide), it is extremely challenging to increase the height of the channel while maintaining a porous membrane between two channels. While maintaining cell separation in chips necessitates the inclusion of a tall porous barrier with closely spaced pores in co-culture environments, traditional photolithographic techniques are not amenable to generating closely-spaced tall features due to the limited height-to-width aspect ratio (5:1).[51]

To overcome this technical challenge, we applied our previously developed backside UV exposure schemes with a selective optical filter [20] to allow the generation of closely-spaced microtrenches in SU-8 master molds (practical height-to-width aspect ratio of 25), and developed modular microfluidic chips with biomaterials. We kept PDMS as the material for our microfluidic layers because of its optical clarity, biocompatibility, flexibility, and amenability for use in high-fidelity replica molding.[52] The molds and microfluidic layers developed using this scheme as well as the assembled microfluidic device with seamlessly incorporated biomaterials are shown in Figures 2 and 3. As reported, microfluidic systems almost always operate in the laminar flow regime leading to predictable fluid dynamics [2]. Our simulations (Figure 4) also predicted laminar fluid streams with minimal mixing between cell chambers while allowing cross-talk between two channels to help maintain ideal culture conditions for both HGKs and HGFs in their respective nutrient media. Under a flow rate of 0.3 μL/min, we generated spatially separated confluent populations of HGKs and HGFs (Figure 4). Altogether, the data revealed that we successfully created spatially separated cell populations that interface with their respective dental material (crown for HGKs and titanium for HGFs) in a new conceptual microfluidic chip.

Another advantage of using a microfluidic approach is the transparency of the materials used in fabrication (most commonly, PDMS and glass). Apart from the usefulness in imaging, this transparency also makes microfluidic devices amenable for use with photobiomodulation (PBM) therapy. PBM therapy has been shown to promote tissue healing and reduce cellular inflammation.[53, 54] In particular, studies have shown that red-to-infrared wavelengths enhance cell proliferation and prevent inflammation of human keratinocytes.[55, 56] In fact, we have previously evaluated near-contact PBM therapy on keratinocytes *in vitro* and investigated its efficacy on host-pathogen interactions.[22] Additionally, we have developed a smart dental implant for PBM therapy on gingival keratinocytes.[31] Thus, the IOC model combined with the PBM therapy module can be a useful tool to test the efficacy of PBM therapy in preventing implant infection and serves as a logical extension of our previous work. Here, we demonstrated the usefulness of PBM therapy in protecting epithelial cells from bacterial invasion (by *S. mutans*) and subsequent damage (Figure 5). Furthermore, the laminar nature of the fluid dynamics in our model prevented the HGF layers from any significant damage by *S. mutans* (Supplementary Figure S10).

Conclusions

In summary, the IOC features potential versatility for various research purposes. Given the microfluidic nature of our model, it is feasible to design multiplexed experimental strategies that can test epithelial invasion by several different pathogens as single species and multispecies. Our proof-of-concept study sets the stage for studying complex, multispecies biofilm formation under clinically relevant settings and testing PBM strategies in such environments. It is also possible to test the effect of exposing the cell-hard tissue interface in implants to different dental monomers. Additionally, to model hypoxic microenvironments, it is possible to decrease the local oxygen concentration in the HGK layer. Furthermore, the PBM amenability of our system can be expanded to incorporate testing of several configurations of LEDs in pulsed or continuous mode. Lastly, our modular fabrication strategy can be extended beyond dentistry to counter the effect of microbe-mediated inflammation on implantable devices placed in extraoral soft and/or hard tissues such as prosthetic joints and limbs. Overall, we present the first, physiologically relevant *in vitro* model of the microenvironment around dental implants for investigation of host-material-pathogen interactions and testing PBM strategies.

Author Contributions

Atul Dhall: Methodology, Investigation, Formal analysis, Data curation, Writing – Original Draft, Writing – Review & Editing, Visualization. **Jun Ying Tan:** Methodology, Investigation. **Min Jun Oh:** Software, Formal analysis, Investigation. **Sayemul Islam:** Investigation, Visualization. **Jungkwun Kim:** Conceptualization, Methodology, Writing – Review & Editing, Supervision, Project administration, Funding acquisition. **Albert Kim:** Conceptualization, Methodology, Writing – Review & Editing,

Supervision, Project administration, Funding acquisition.Investigation. **Geelsu Hwang:** Conceptualization, Methodology, Writing – Review & Editing, Supervision, Project administration, Funding acquisition.

Conflicts of interest

There are no conflicts to declare.

Acknowledgements

We would like to thank Dr. Korostoff and Dr. Graves at the School of Dental Medicine, University of Pennsylvania for providing HGF and HGK cells, respectively.

This work was financially supported by the National Institutes of Health, National Institute of Dental and Craniofacial Research grant DE027970 and National Science Foundation grant ECCS-2225697 (GH), National Science Foundation grant ECCS-2029077, ECCS-2054492, and ECCS-2225681 (AK), and National Science Foundation grant ECCS-2029086 and ECCS-2054567 (JK). Minjun Oh is a recipient of the Basic Science Research Program through the National Research Foundation of Korea funded by the Ministry of Education (NRF-2021R1A6A3A03044553).

References

1. K. W. Oh, *Journal*, 2017, **8**, 343.
2. E. K. Sackmann, A. L. Fulton and D. J. Beebe, *Nature*, 2014, **507**, 181-189.
3. B. Zhang, A. Korolj, B. F. L. Lai and M. Radisic, *Nature Reviews Materials*, 2018, **3**, 257-278.
4. K. Duval, H. Grover, L.-H. Han, Y. Mou, A. F. Pegoraro, J. Fredberg and Z. Chen, *Physiology*, 2017, **32**, 266-277.
5. H. J. Kim, D. Huh, G. Hamilton and D. E. Ingber, *Lab on a Chip*, 2012, **12**, 2165-2174.
6. J.-M. Prot, A. Bunescu, B. Elena-Herrmann, C. Aninat, L. C. Snouber, L. Griscom, F. Razan, F. Y. Bois, C. Legallais and C. Brochot, *Toxicology and applied pharmacology*, 2012, **259**, 270-280.
7. D. Huh, D. C. Leslie, B. D. Matthews, J. P. Fraser, S. Jurek, G. A. Hamilton, K. S. Thorneloe, M. A. McAlexander and D. E. Ingber, *Science translational medicine*, 2012, **4**, 159ra147-159ra147.
8. Y.-s. Torisawa, C. S. Spina, T. Mammoto, A. Mammoto, J. C. Weaver, T. Tat, J. J. Collins and D. E. Ingber, *Nature methods*, 2014, **11**, 663-669.
9. J. Seo, W. Y. Byun, A. Frank, M. Massaro-Giordano, V. Lee, V. Y. Bunya and D. Huh, *Investigative Ophthalmology & Visual Science*, 2016, **57**, 3872-3872.
10. A. Guan, Y. Wang, K. S. Phillips and Z. Li, *Lab on a Chip*, 2016, **16**, 1152-1156.
11. F. Sharifi, S. S. Htwe, M. Righi, H. Liu, A. Pietralunga, O. Yesil-Celiktas, S. Maharjan, B. H. Cha, S. R. Shin and M. R. Dokmeci, *Advanced healthcare materials*, 2019, **8**, 1801425.
12. J. Tillander, K. Hagberg, L. Hagberg and R. Brånemark, *Clinical Orthopaedics and Related Research®*, 2010, **468**, 2781-2788.
13. B. Klinge, M. Hultin and T. Berglundh, *Dental Clinics*, 2005, **49**, 661-676.
14. J. S. Dhaliwal, N. A. Abd Rahman, L. C. Ming, S. K. S. Dhaliwal, J. Knights and R. F. Albuquerque Junior, *Frontiers in cellular and infection microbiology*, 2021, 922.
15. P. Sahrmann, F. Gilli, D. B. Wiedemeier, T. Attin, P. R. Schmidlin and L. Karygianni, *Microorganisms*, 2020, **8**, 661.
16. H. Elani, J. Starr, J. Da Silva and G. Gallucci, *Journal of dental research*, 2018, **97**, 1424-1430.
17. S. R. Dutta, D. Passi, P. Singh, M. Atri, S. Mohan and A. Sharma, *National Journal of Maxillofacial Surgery*, 2020, **11**, 14.
18. A. Hanif, S. Qureshi, Z. Sheikh and H. Rashid, *European journal of dentistry*, 2017, **11**, 135-140.
19. R. Pokrowiecki, A. Mielczarek, T. Zaręba and S. Tyski, *Therapeutics and clinical risk management*, 2017, **13**, 1529.
20. J. J. Kim, H. Al Thuwaini and M. Almuslem, *Micro and Nano Systems Letters*, 2018, **6**, 1-9.
21. F. Pisapia, W. Balachandran and M. Rasekh, *Applied Sciences*, 2022, **12**, 3829.
22. H. E. Kim, S. Islam, M. Park, A. Kim and G. Hwang, *Advanced Biosystems*, 2020, **4**, 1900227.
23. H. Kim, A. Dhall, Y. Liu, M. Bawazir, H. Koo and G. Hwang, *Mbio*, 2021, **12**, e00651-00621.
24. A. Dhall, S. Islam, M. Park, Y. Zhang, A. Kim and G. Hwang, *ACS Applied Materials & Interfaces*, 2021, **13**, 40379-40391.
25. J. Schindelin, I. Arganda-Carreras, E. Frise, V. Kaynig, M. Longair, T. Pietzsch, S. Preibisch, C. Rueden, S. Saalfeld and B. Schmid, *Nature methods*, 2012, **9**, 676-682.
26. L. Amato, S. S. Keller, A. Heiskanen, M. Dimaki, J. Emnéus, A. Boisen and M. Tenje, *Microelectronic engineering*, 2012, **98**, 483-487.
27. K. L. Ly, S. A. Rooholghodos, C. Rahimi, B. Rahimi, D. R. Bienek, G. Kaufman, C. B. Raub and X. Luo, *Biomedical Microdevices*, 2021, **23**, 1-11.
28. W. Liu, L. Li, X. Wang, L. Ren, X. Wang, J. Wang, Q. Tu, X. Huang and J. Wang, *Lab on a Chip*, 2010, **10**, 1717-1724.
29. T. Agarwal, G. H. Narayana and I. Banerjee, *Cytoskeleton*, 2019, **76**, 209-218.
30. K. D. Peck, A. H. Ghanem and W. I. Higuchi, *Pharm. Res.*, 1994, **11**, 1306-1314.
31. M. Park, S. Islam, H. E. Kim, J. Korostoff, M. B. Blatz, G. Hwang and A. Kim, *Advanced Healthcare Materials*, 2020, **9**, 2000658.
32. L. A. Low, C. Mummery, B. R. Berridge, C. P. Austin and D. A. Tagle, *Nature Reviews Drug Discovery*, 2021, **20**, 345-361.
33. A. Guan, P. Hamilton, Y. Wang, M. Gorbet, Z. Li and K. S. Phillips, *Nature Biomedical Engineering*, 2017, **1**, 1-10.
34. A. P. M. Guttenplan, Z. Tahmasebi Birgani, S. Giselbrecht, R. K. Truckenmüller and P. Habibović, *Advanced Healthcare Materials*, 2021, **10**, 2100371.
35. G. A. Van Norman, *JACC Basic Transl Sci*, 2019, **4**, 845-854.
36. J. Seok, H. S. Warren, A. G. Cuenca, M. N. Mindrinos, H. V. Baker, W. Xu, D. R. Richards, G. P. McDonald-Smith, H. Gao and L. Hennessy, *Proceedings of the National Academy of Sciences*, 2013, **110**, 3507-3512.
37. N. Dhiman, P. Kingshott, H. Sumer, C. S. Sharma and S. N. Rath, *Biosensors and Bioelectronics*, 2019, **137**, 236-254.
38. R. Dong, Y. Liu, L. Mou, J. Deng and X. Jiang, *Advanced Materials*, 2019, **31**, 1805033.

39. J. H. Tsui, W. Lee, S. H. Pun, J. Kim and D.-H. Kim, *Advanced drug delivery reviews*, 2013, **65**, 1575-1588.
40. S. S. Socransky and A. D. Haffajee, *Journal of periodontology*, 1992, **63**, 322-331.
41. L. Niu, H. Zhang, Y. Liu, Y. Wang, A. Li, R. Liu, R. Zou and Q. Yang, *ACS Biomaterials Science & Engineering*, 2019, **5**, 4844-4851.
42. C. M. França, A. Tahayeri, N. S. Rodrigues, S. Ferdosian, R. M. P. Rontani, G. Sereda, J. L. Ferracane and L. E. Bertassoni, *Lab on a Chip*, 2020, **20**, 405-413.
43. C. Rahimi, B. Rahimi, D. Padova, S. A. Rooholghodos, D. R. Bienek, X. Luo, G. Kaufman and C. B. Raub, *Biomicrofluidics*, 2018, **12**, 054106.
44. N. S. Rodrigues, C. M. França, A. Tahayeri, Z. Ren, V. P. Saboia, A. J. Smith, J. L. Ferracane, H. Koo and L. E. Bertassoni, *Journal of dental research*, 2021, **100**, 1136-1143.
45. L. Palomo and G. T. Terézhalmy, *Provider*, 2014, **501**, 211886.
46. P. Rosen, D. Clem, D. L. Cochran, S. Froum, B. McAllister, S. Renvert and H. L. Wang, *Journal of periodontology*, 2013, **84**, 436-443.
47. S. Sakka, K. Baroudi and M. Z. Nassani, *Journal of investigative and clinical dentistry*, 2012, **3**, 258-261.
48. G. Charalampakis, Å. Leonhardt, P. Rabe and G. Dahlén, *Clinical oral implants research*, 2012, **23**, 1045-1054.
49. X. Li, N. Wu, Y. Rojanasakul and Y. Liu, *Sensors and Actuators A: Physical*, 2013, **193**, 186-192.
50. E. W. Young and D. J. Beebe, *Chemical Society Reviews*, 2010, **39**, 1036-1048.
51. K. Microchem, *Kayaku Microchem*, 2019.
52. S. K. Sia and G. M. Whitesides, *Electrophoresis*, 2003, **24**, 3563-3576.
53. R. J. Lanzafame, I. Stadler, A. F. Kurtz, R. Connelly, P. Brondon and D. Olson, *Lasers in Surgery and Medicine: The Official Journal of the American Society for Laser Medicine and Surgery*, 2007, **39**, 534-542.
54. M. R. Hamblin, *AIMS biophysics*, 2017, **4**, 337.
55. Y.-H. Hsu, Y.-F. Lin, C.-H. Chen, Y.-J. Chiu and H.-W. Chiu, *Journal of Molecular Medicine*, 2017, **95**, 1203-1213.
56. Q. Sun, H.-E. Kim, H. Cho, S. Shi, B. Kim and O. Kim, *Journal of Photochemistry and Photobiology B: Biology*, 2018, **186**, 31-40.